Agricultural and Forest Meteorology 341 (2023) 109658

Contents lists available at ScienceDirect

Agricultural and Forest Meteorology

journal homepage: www.elsevier.com/locate/agrformet

Improving the ability of solar-induced chlorophyll fluorescence to track gross primary production through differentiating sunlit and shaded leaves

Zhaoying Zhang [a,b,d,*], Jing M. Chen [c], Yongguang Zhang [a,b,d], Manchun Li [b,*]

[a] Jiangsu Center for Collaborative Innovation in Geographical Information Resource Development and Application, International Institute for Earth System Sciences, Nanjing University, Nanjing, Jiangsu 210023, China
[b] Jiangsu Provincial Key Laboratory of Geographic Information Science and Technology, Key Laboratory for Land Satellite Remote Sensing Applications of Ministry of Natural Resources, School of Geography and Ocean Science, Nanjing University, Nanjing, Jiangsu, China
[c] Department of Geography and Planning, University of Toronto, Toronto, Ontario, Canada
[d] International Joint Carbon Neutrality Laboratory, Jiangsu, China

ARTICLE INFO

Keywords:
SIF
GPP
Sunlit leaves
Shaded leaves
TROPOMI

ABSTRACT

Recently, solar-induced chlorophyll fluorescence (SIF) is a promising tool to estimate gross primary production (GPP). Photosynthesis gradually saturates with the increasing light, but fluorescence tends to keep increasing, leading to a nonlinear SIF-GPP relationship. This nonlinearity occurs for sunlit leaves but not for shaded leaves for which photosynthesis is light-limited. However, the separation of sunlit and shaded SIF has not been systematically investigated when estimating GPP from SIF. Therefore, it is promising to develop a model for GPP estimation considering such differences. This study proposed an approach to separate the total canopy SIF emission (SIF_{total}) from TROPOspheric Monitoring Instrument (TROPOMI) SIF into their sunlit and shaded components (SIF_{sun} and SIF_{shade}). The nonlinearity and linearity in SIF-GPP relationships for sunlit and shaded leaves were incorporated into a two-leaf hybrid model, which was fitted using flux tower data and then evaluated using leave-one-site-out crossing validation. We also elucidated the distinct SIF-GPP relationships between sunlit and shaded leaves using the Soil-Canopy-Observation of Photosynthesis and the Energy balance (SCOPE) model simulation. Compared to previously used linear ($R^2 = 0.68$, RMSE = 2.13 $gC{\cdot}m^{-2}{\cdot}d^{-1}$) or hyperbolic ($R^2 = 0.72$, RMSE = 2.01 $gC{\cdot}m^{-2}{\cdot}d^{-1}$) model based on the big-leaf assumption, our proposed two-leaf hybrid model has the best performance on GPP estimation ($R^2 = 0.77$, RMSE = 1.79 $gC{\cdot}m^{-2}{\cdot}d^{-1}$). We also applied this two-leaf hybrid model to estimate the global GPP during the main growing season in Northern Hemisphere, which were highly correlated with several existing GPP products, with R^2 ranging from 0.79 to 0.88. These results will improve our understanding of the relationship between SIF and GPP for sunlit and shaded leaves and will advance application of satellite SIF data to GPP estimation.

1. Introduction

Solar-induced chlorophyll fluorescence (SIF), which is emitted by chlorophyll-a during the photosynthetic process (Krause and Weis, 1991; Meroni et al., 2009), has been a promising remotely sensible parameter to estimate terrestrial gross primary production (GPP) across multiple spatial and temporal scales (Frankenberg et al., 2011; Damm et al., 2015; Sun et al., 2017; Li et al., 2018). Recently, several studies have used satellite SIF to estimate regional or global GPP either by directly using their statistical relationships (Guanter et al., 2014; Li and Xiao, 2019; Zhang et al., 2020a) or constraining process-based models (Lee et al., 2015; MacBean et al., 2018; Norton et al., 2018).

The direct linear or nonlinear model is widely adopted in calibrating the relationship between SIF and GPP due to its efficiency (Frankenberg et al., 2011; Sun et al., 2017; Maguire et al., 2020; Liu et al., 2022). Although the relationship between SIF and GPP is nonlinear in theory (Gu et al., 2019), the practical use of linear or nonlinear model depends on multiple factors, such as photosynthesis pathway (He et al., 2020; Zhang et al., 2020b), spatiotemporal scales (Zhang et al., 2016; Magney et al., 2020), and the ratio between the sunlit and shaded portion of the canopy (Liu et al., 2022). For example, the nonlinear relationship between SIF and GPP tends to be linear when the SIF and GPP are averaged

* Corresponding authors at: Jiangsu Provincial Key Laboratory of Geographic Information Science and Technology, Key Laboratory for Land Satellite Remote Sensing Applications of Ministry of Natural Resources, School of Geography and Ocean Science, Nanjing University, Nanjing, Jiangsu, China.
E-mail addresses: zhaoying_zhang@nju.edu.cn (Z. Zhang), limanchun@nju.edu.cn (M. Li).

https://doi.org/10.1016/j.agrformet.2023.109658
Received 5 June 2023; Received in revised form 8 August 2023; Accepted 10 August 2023
Available online 23 August 2023

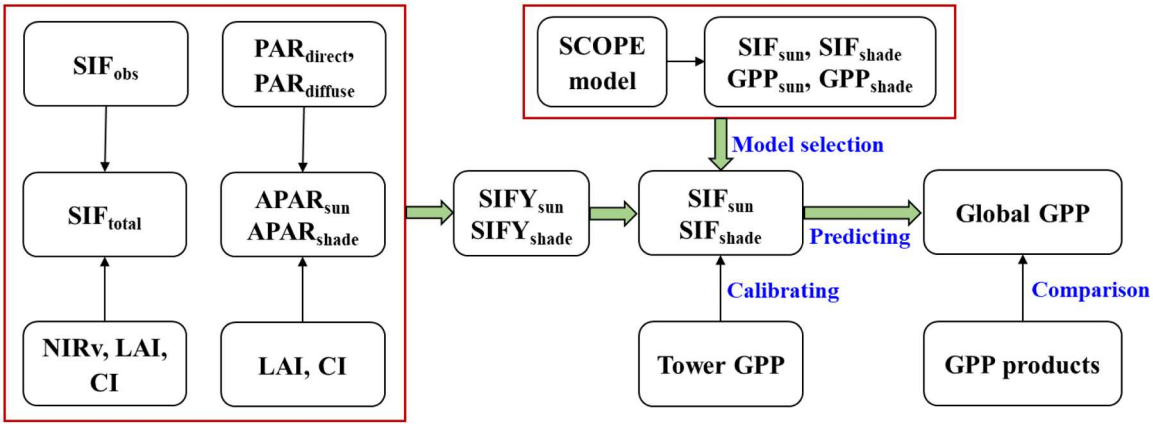

Fig. 1. Flowchart used in this study. Key steps were shown in green arrows for better visualization. Details about the input parameters can be found in the following sections.

Table 1
The input parameters of the SCOPE model simulations.

Parameter	Meaning	Value
Cab (ug·cm^{-2})	Chlorophyll content	40
Cca (ug·cm^{-2})	Carotenoid content	10
Cdm (g·cm^{-2})	Dry matter content	0.0012
Cw (g·cm^{-2})	Water content	0.009
N	Leaf thickness parameters	1.5
Vcmax25 (umol·m^{-2}·s^{-1})	Maximum carboxylation capacity	40 and 80
LIDFa, LIDFb	Leaf inclination and variation	Planophile (1, 0), Erectophile (−1, 0), Plagiophile (0, −1), Extremophile (0, 1), Sphereical (−0.35, −0.15), Uniform (0, 0)
LAI (m^2·m^{-2})	Leaf area index	6
Rin (W·m^{-2})	Incoming shortwave radiation (0.4–2.5 um)	10–600
Fqe	Fluorescence quantum yield efficiency at photosystem level	0.01

from the hourly scale to the weekly or longer scale (Zhang et al., 2016; Pierrat et al., 2022). Regardless of the linear or nonlinear model, these studies mainly considered the canopy as a whole and aggregated photosynthesis and fluorescence into a single element: the so-called big-leaf model. However, the big-leaf model may not accurately capture the quantum response of leaf photosynthesis due to the vertical heterogeneity of absorbed irradiance and photosynthetic capacity, as demonstrated by many authors (Pury and Farquhar, 1997; Wang and Leuning, 1998; Guan et al., 2021).

Although fluorescence is intrinsically linked to photochemical efficiency and can be used to track the plant photochemistry (Genty et al., 1989; Porcar-Castell et al., 2014, 2021), fluorescence and photosynthesis are not identical in response to the variation in illumination. Under the clear sky, the photosynthesis rate is light-saturated for the upper leaves (such as sunlit leaves) but light-limited for the bottom leaves (such as shaded leaves), however, fluorescence is nearly linearly related to absorbed radiation (van der Tol et al., 2009a; Damm et al., 2015; Zhang et al., 2016; Gu et al., 2019). These indicate that sunlit and shaded leaves may have different SIF-GPP relationships and such differences cannot be captured by the big-leaf model that just represents the averaged conditions.

To address the aforementioned issue, a possible strategy is to separate all leaves into sunlit and shaded components (Pury and Farquhar, 1997; Leuning et al., 1998; Wang and Leuning, 1998; Chen et al., 1999) and this strategy has been also incorporated into the two-leaf light use efficiency model (TL-LUE) (Zhou et al., 2016; Xie and Li, 2020; Guan et al., 2021; Bi et al., 2022). Recently, several studies have suggested to separately model the sunlit and shaded component of SIF (Sun et al., 2023) and the Community Land Model version 5 has implemented the a single-layer two leaf representation of SIF (Li et al., 2022). However, to the best of our knowledge, none of studies have considered the difference in SIF-GPP relationships between sunlit and shaded leaves in practice due to the lack of observations of sunlit and shaded SIF and GPP. The only related study was conducted by He et al. (2017) who derived sunlit and shaded SIF based on the geometric-optical model, but they did not investigate the model difference in SIF-GPP relationships between shaded and sunlit leaves.

Therefore, it is promising to estimate GPP from SIF considering the difference in SIF-GPP relationships between sunlit and shaded leaves. Since sunlit and shaded SIF and GPP cannot be directly observed, the Soil-Canopy-Observation of Photosynthesis and the Energy balance (SCOPE) model (van der Tol et al., 2009b) provides a unique tool to investigate the mechanistical link between SIF and GPP for sunlit and shaded leaves separately. Furthermore, the knowledge obtained from the SCOPE model simulation can be applied to actual scenarios for GPP estimation. The objectives of this study were (1) to explore the differences in SIF-GPP relationships between sunlit and shaded leaves using the SCOPE model, (2) to propose an approach to deriving sunlit and shaded SIF from observed SIF, and (3) to establish a model for GPP estimation based on sunlit and shaded SIF.

2. Materials and methods

The overall flowchart used in this study is shown in Fig. 1, mainly including four steps: (1) the choice of the fitting function between GPP and SIF for sunlit and shaded leaves based on the SCOPE model, (2) the estimation of SIF yields at photosystem level for sunlit and shaded leaves ($SIFY_{sun}$ and $SIFY_{shade}$), (3) the estimation of SIF for sunlit and shaded leaves (SIF_{sun} and SIF_{shade}), and (4) the GPP model calibration based SIF_{sun} and SIF_{shade}, The first step was presented in Section 2.1, the second and third steps were presented in Section 2.2, and the fourth step was presented in Section 2.3. The description of SIF and GPP were presented in Sections 2.4 and 2.5, respectively.

2.1. SCOPE model simulation

The SCOPE v2.0 model (van der Tol et al., 2009b; Yang et al., 2021) was used to simulate the sunlit and shaded SIF and GPP. The SCOPE model can simulate absorption and scattering of SIF with meteorological, structural, biochemical parameters as well as a given sun-target-viewing geometry. The main parameters were listed in Table 1 and other input parameters were set to their default values in the original SCOPE model. The relationships between SIF and GPP were

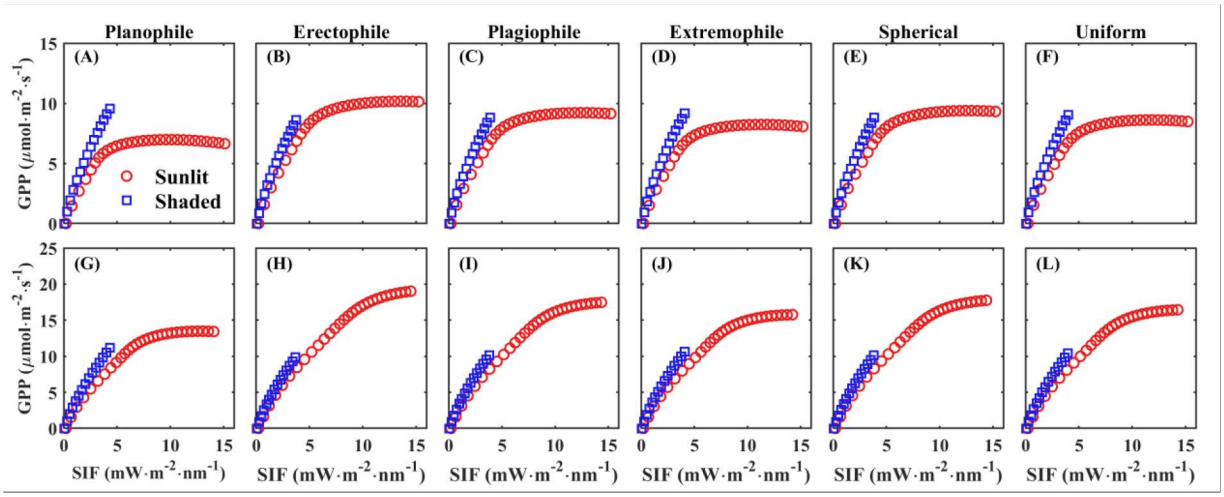

Fig. 2. Scattering plots of SIF and GPP for sunlit (red circle) and shaded (blue square) leaves based on the SCOPE model simulations for different leaf angle distributions: (A) planophile, (B) erectophile, (C) plagiophile, (D) extremophile, (E) spherical, and (F) uniform under the V_{cmax} of 40 μmol·m^{-2}·s^{-1}. (G-L) Similar to (A-F) but for the V_{cmax} of 80 μmol·m^{-2}·s^{-1}.

compared for sunlit and shaded leaves, separately (Fig. 2). In particular, we analyzed the effects of maximum carboxylation capacity (V_{cmax}) on the relationship between SIF and GPP due to its vital importance for photosynthesis (van der Tol et al., 2014; Zhang et al., 2016). Different leaf angle distributions (LiDFa, LIDFb) were also considered. We used a relative high LAI (6) to better visualize the difference in the model for SIF and GPP between sunlit and shaded leaves. When the incoming shortwave radiation (Rg) exceeds 800 W·m^{-2}, we found the simulated GPP starts to decline. Therefore, we only used the Rg in the range of 10 – 600 W·m^{-2}. In addition, we also observed negative GPP output from the SCOPE model under the weak illumination (such as 10 W·m^{-2}). Therefore, we subtracted the minimal GPP from the simulated GPP for both sunlit and shaded leaves to keep the minimal GPP as zero.

The relationships between SIF and GPP for sunlit and shaded leaves are simulated separately using SCOPE (Fig. 2). GPP_{sun} quickly transited from being light limited to light saturated at the low level of V_{cmax} (40 μmol·m^{-2}·s^{-1}) and thus exhibited clear nonlinearity for all leaf angle distributions (Fig. 2A-F). The point at which this transition occurred was larger at the higher level of V_{cmax} (80 μmol·m^{-2}·s^{-1}), weakening the nonlinearity for SIF_{sun} and GPP_{sun} to some extent (Fig. 2G-L). However, linear relationships were observed from GPP_{shade} and SIF_{shade} regardless of the level of V_{cmax}. These results indicate that there are clear differences in SIF-GPP relationships between sunlit and shaded leaves, especially for the low level of V_{cmax}.

2.2. Separation of sunlit and shaded leaves

The separation of sunlit SIF (SIF_{sun}) and shaded SIF (SIF_{shade}) was achieved in two steps. The first step was to derive the total canopy SIF emission (SIF_{total}) before scattering and reabsorption from the observed SIF (SIF_{obs}) using the reflectance-based methods as below:

$$SIF_{total} = \frac{SIF_{obs}}{f_{esc}} \tag{1}$$

$$f_{esc} = \frac{NIR_V}{\pi \times i_0 \times K_\lambda} \tag{2}$$

where f_{esc} is the probability of fluorescence escaping from canopy and NIR_V is the near-infrared reflectance of vegetation (Badgley et al., 2017, 2019). NIR_V is calculated with the reflectance at red (R) and near-infrared (NIR) bands that should be in the same sun-view geometry of TROPMI SIF_{obs}. In this study, R and NIR were simulated by driving the RossThick-LiSparseR model using the MODIS BRDF parameters that were provided by MCD19A3 (Lyapustin et al., 2011, 2018). i_0 was derived with the G-function, leaf area index (LAI), clumping index (CI), and solar zenith angle (SZA, θ). MODIS LAI was obtained from MCD15A2H (Myneni et al., 2002) and CI was obtained from (He et al., 2012). All satellite products were aggregated into 0.2° grids for spatial consistency. K_λ is ratio of leaf albedo to the escape probability of fluorescence from photosystem to leaf surface at 740 nm and was set as 1.2 for far-red SIF (Zhang et al., 2021). A comprehensive description of f_{esc} and its uncertainty can be found in Zhang et al. (2021).

In the second step, SIF_{total} was used to directly separate SIF_{sun} and SIF_{shade} because SIF_{total} is insensitive to the canopy structural and angular effects (Yang and van der Tol, 2018; Zeng et al., 2019; Liu et al., 2020; Zhang et al., 2021) and can simplify the separation process. Analogous to the LUE model, SIF_{sun} and SIF_{shade} can be expressed as below:

$$SIF_{sun} = APAR_{sun} \times SIFY_{sun} \tag{3}$$

$$SIF_{shade} = APAR_{shade} \times SIFY_{shade} \tag{4}$$

$$SIF_{total} = APAR_{sun} \times SIFY_{sun} + APAR_{shade} \times SIFY_{shade} \tag{5}$$

where $APAR_{sun}$ and $APAR_{shade}$ are the PAR absorbed by sunlit and shaded leaves, respectively. $SIFY_{sun}$ and $SIFY_{shade}$ are the SIF yield at photosystem level for sunlit and shaded leaves, respectively.

We calculated $APAR_{sun}$ and $APAR_{shade}$ according to previous studies (Chen et al., 1999; Bi et al., 2022):

$$APAR_{shade} = \left(\frac{PAR_{diffuse} - PAR_{diffuse,\ u}}{LAI} + \mathrm{C}\right) \times LAI_{shade} \tag{6}$$

$$APAR_{sun} = \left(\frac{PAR_{dir}\cos\beta}{LAI} + \frac{PAR_{diffuse} - PAR_{diffuse,\ u}}{LAI} + \mathrm{C}\right) \times LAI_{sun} \tag{7}$$

$$LAI_{sun} = 2\cos SZA \times \left[1 - \exp\left(-\frac{LAI \times CI}{2\cos\theta}\right)\right] \tag{8}$$

$$LAI_{shade} = LAI - LAI_{sun} \tag{9}$$

$$\mathrm{C} = 0.07 \times \mathrm{CI} \times PAR_{dir} \times (1.1 - 0.1 \times \mathrm{LAI}) \times \exp(-\cos\theta) \tag{10}$$

$$PAR_{diffuse,u} = PAR_{diffuse} \times \exp\left(-\frac{0.5 \times LAI \times CI}{0.537 + 0.025 \times LAI}\right) \tag{11}$$

where PAR_{direct} and $PAR_{diffuse}$ are the direct and diffuse PAR, respec-

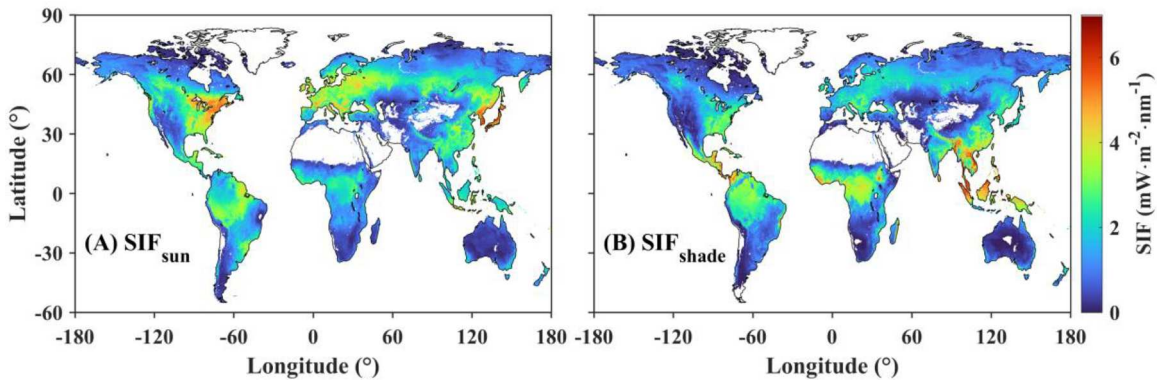

Fig. 3. Global map of (A) SIF_{sun} and (B) SIF_{shade} derived from TROPOMI averaged over May to September in 2018.

tively. PAR_{direct} and $PAR_{diffuse}$ were obtained by interpolating the MERRA-2 reanalysis data (Gelaro et al., 2017). $PAR_{diffuse,u}$ is the diffuse PAR reaching to the ground. β is the mean leaf-sun angle, which is set as 60°, a good approximation in θ from 30 to 60° (Chen et al., 1999; Bi et al., 2022).

$SIFY_{sun}$ and $SIFY_{shade}$ are unknown but can be estimated. Assuming $SIFY_{sun}$ and $SIFY_{shade}$ are constant or change slowly during a fixed period, the combination equation (Eq. (12)) can be used to estimate $SIFY_{sun}$ and $SIFY_{shade}$ using the least square method. More details about the least square method can be found in Text A1 in the Appendix. Once $SIFY_{sun}$ and $SIFY_{shade}$ were estimated, SIF_{sun} and SIF_{shade} can be estimated using Eqs. (3) and (4).

$$\begin{aligned} SIF^1_{total} &= APAR^1_{sun} \times SIFY_{sun} + APAR^1_{shade} \times SIFY_{shade} \\ &\vdots \\ SIF^N_{total} &= APAR^N_{sun} \times SIFY_{sun} + APAR^N_{shade} \times SIFY_{shade} \end{aligned} \tag{12}$$

where N is the number of day when TROPOMI SIF was available during a fixed period. To increase the stability of the estimated $SIFY_{sun}$ and $SIFY_{shade}$, we solved Eq. (12) in a 16-day interval and 1° × 1° moving window assuming the environmental conditions were similar.

2.3. GPP estimation model based on sunlit and shaded SIF

Based on the SCOPE model simulations, nonlinear and linear models were used to fit the SIF-GPP relationship for sunlit and shaded leaves, respectively (see Section 2.1). For sunlit leaves, the hyperbolic model proposed by Damm et al. (2015) was used to account for the saturation. Because the sunlit and shaded GPP were not available from the flux tower, the model coefficients were not fitted for sunlit and shaded leaves separately. On the contrary, we directly fitted the model for the whole canopy GPP as Eq. (13) (denoted as a two-leaf hybrid model). For comparison purpose, the GPP estimation models directed based on SIF_{total} using linear or hyperbolic model were also considered, denoted as a big-leaf linear (Eq. (14)) or hyperbolic (Eq. (15)) model, respectively.

$$GPP = (a_1 \times SIF_{sun})/(SIF_{sun} + a_2) + (a_3 \times SIF_{shade} + a_4) \tag{13}$$

$$GPP = a_5 \times SIF_{total} + a_6 \tag{14}$$

$$GPP = (a_7 \times SIF_{total})/(SIF_{total} + a_8) \tag{15}$$

2.4. TROPOMI SIF data

TROPOMI onboard the Sentinel-5 Precursor satellite is an imaging spectrometer, which collects the spectral data at an improved spatial resolution (5.6 km × 3.5 km and 5.6 km × 3.5 km at nadir after August 6, 2019), with a wide swath of approximately 2600 km that allows for almost daily surface coverage. Due to its high spectral resolution in the spectral region overlapping with the solar Fraunhofer lines, SIF has been successfully retrieved with a singular value decomposition (SVD) technique (Köhler et al., 2018b; Guanter et al., 2021). This study adopted SIF that was retrieved by the ESA-TROPOSIF team using the spectral range of 743–758 nm (Guanter et al., 2021). The retrieved SIF was normalized to 740 nm using a reference fluorescence spectrum. SIF observations with a cloud fraction larger than 0.2 were excluded and then the remaining SIF observations were aggregated into 0.2° grids for each day. Averaging multiple individual observations into a single value would effectively reduce the retrieval noise of SIF (Frankenberg et al., 2014; Yu et al., 2019). Therefore, we only used these 0.2° grids averaged from at least six observations. We used the TROPOMI SIF from May 2018 to December 2021 and presented the spatial patterns during May to September (when the fraction of green vegetation is maximal) in 2018 as an example. The instantaneous SIF_{sun} and SIF_{shade} at the overpass time of TROPOMI SIF were derived using Eq. (12). The daily mean SIF_{sun} and SIF_{shade} were obtained by converting the instantaneous fluorescence to daily averages following the method of Frankenberg et al. (2011).

2.5. Tower and global GPP data

Two types of GPP data were used in this study: tower GPP estimated from tower-based measurements and multiple global GPP products that are available in 2018. The tower flux data at 45 sites from AmeriFlux (http://ameriflux.ornl.gov/), European Flux Database (www.europe-fluxdata.eu/home), and OzFlux (http://data.ozflux.org.au/portal/home), were used after checking the land homogeneity and data availability from 2018 to 2021 and their information can be found in Table A1. The half-hourly GPP was obtained by partitioning the measured net ecosystem exchange of carbon dioxide based on the nighttime partitioning approach Reichstein et al., 2005). The half-hourly GPP was averaged into the daily GPP to fit the GPP models (Eqs. (13)–(15)). The estimation accuracy was evaluated using the widely leave-one-site-out cross-validation strategy (Bodesheim et al., 2018; Joiner et al., 2018). Only sites with C_3 plants were considered for simplicity because the latest global fractional map of C_4 plants was not available.

The best model from Eqs. (13)–(15) was used to estimate the global GPP by applying the model to each 0.2° grid. Then, the estimated GPP was averaged for each monthly from May 2018 to December 2020. The estimated GPP from SIF was then compared with five global GPP products, including TL-LUE (Bi et al., 2022), VPM (Zhang et al., 2017), PML v2 (Zhang et al., 2019), FLUXCOM (Tramontana et al., 2016), and FluxSat v2 (Joiner and Yoshida, 2020). The details about these products can be found in the cited references. In particular, the TL-LUE model also provided the global sunlit and shaded GPP (Bi et al., 2022), which were compared with the derived TROPOMI sunlit and shaded SIF (see Section 3.2). All these GPP products were spatially aggregated into 0.2° grids, except for FLUXCOM that was originally provided in 0.5° grids.

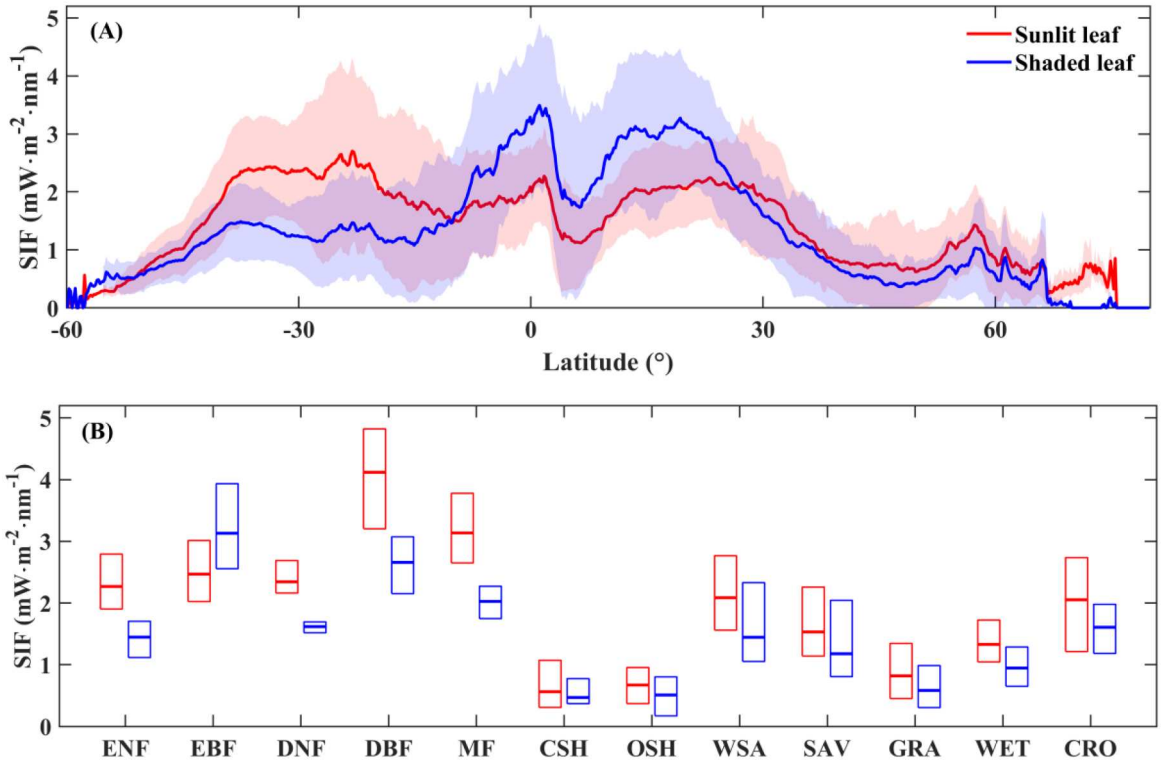

Fig. 4. (A) Latitudinal patterns of SIF_{sun} and SIF_{shade}, with the shaded area indicating the standard deviation. (B) Box plots of SIF_{sun} and SIF_{shade} per vegetation type. Data was obtained from Fig. 3.

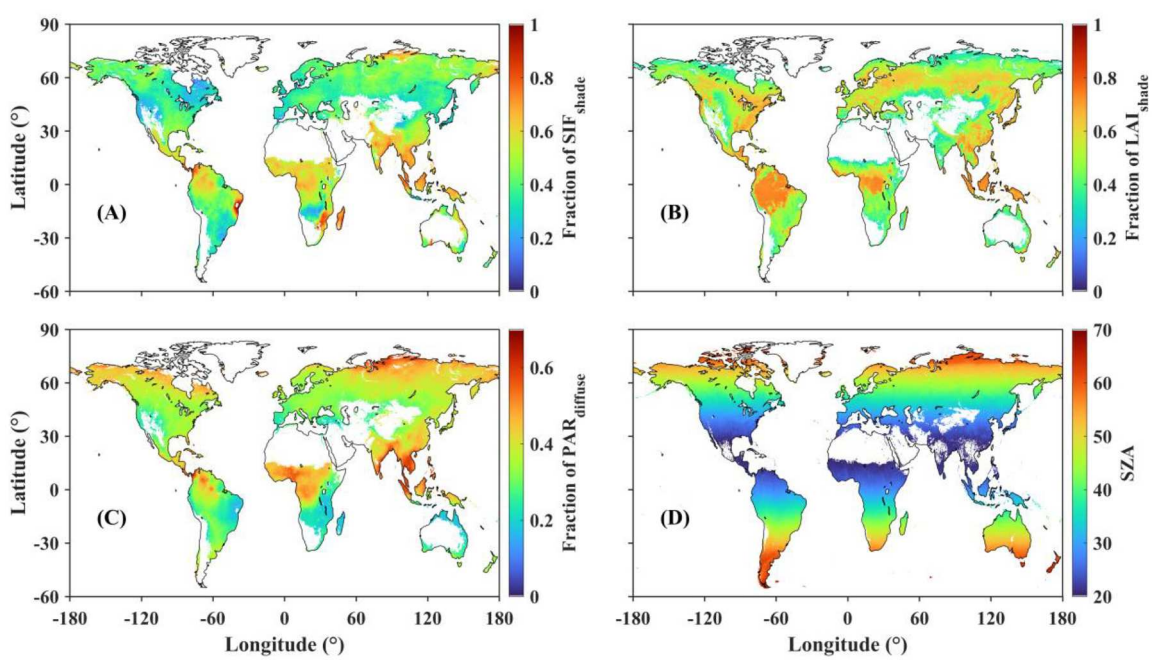

Fig. 5. Global fractions of (A) SIF_{shade}, (B) LAI_{shade}, and (C) $PAR_{diffuse}$ averaged over May to September in 2018. (D) Global pattern of solar zenith angle (SZA) at the overpass time of TROPOMI.

Therefore, the GPP estimated from SIF can be compared with GPP from TL-LUE, VPM, PML v2, and FluxSat v2 in a consistent spatial resolution.

3. Results

3.1. Global map of SIF_{sun} and SIF_{shade} from TROPOMI

The global maps of SIF_{sun} and SIF_{shade} derived from TROPOMI SIF averaged over May to September in 2018 are shown in Fig. 3. The spatial

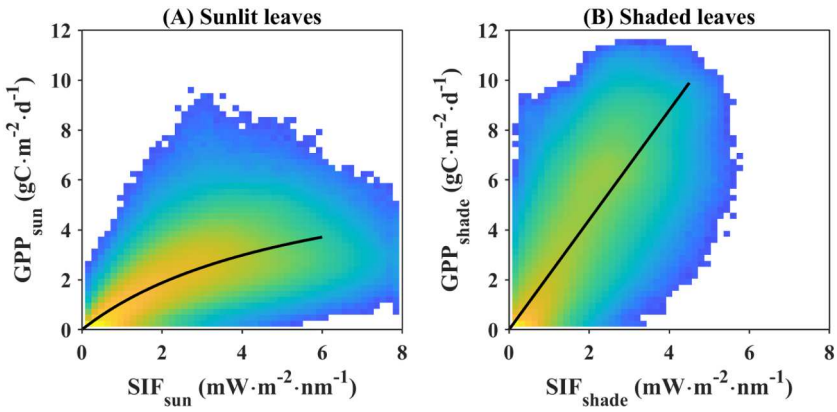

Fig. 6. Density plots of SIF and GPP for (A) sunlit and (B) shaded leaves. SIF_{sun} and SIF_{shade} were derived from TROPOMI and GPP_{sun} and GPP_{shade} were obtained from TL-LUE.

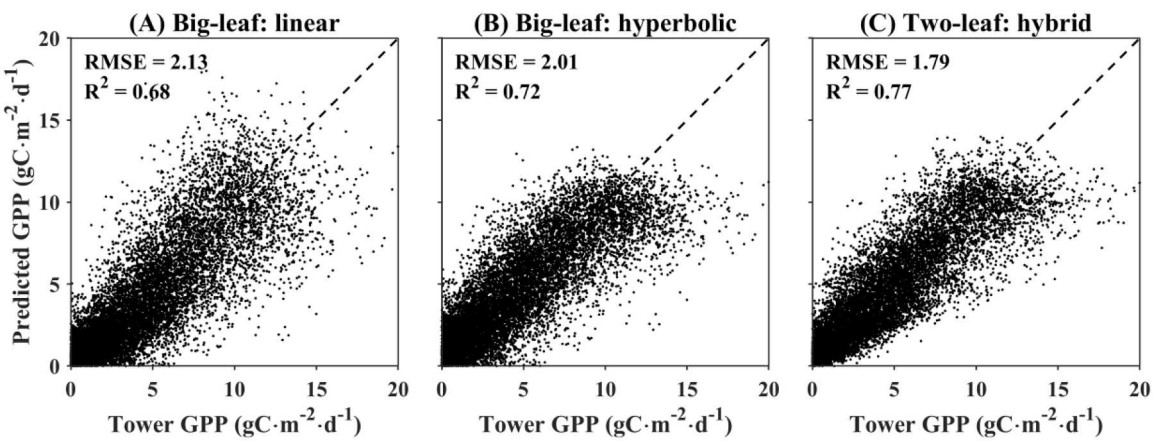

Fig. 7. Comparisons of tower GPP and GPP estimated from (A) a big-leaf-based linear model, (B) a big-leaf based hyperbolic model, and (C) a two-leaf-based hybrid model using the leave-one-site-out crossing validation. The black dotted lines represent the 1:1 line.

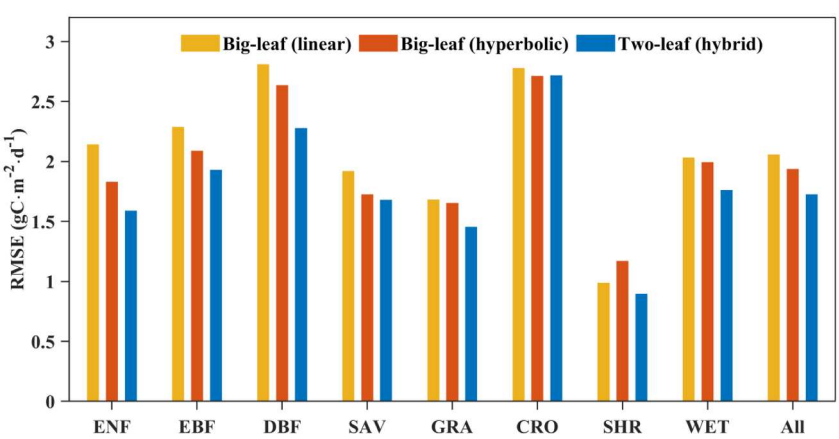

Fig. 8. Comparison of RMSE for the big-leaf linear model, big-leaf hyperbolic model, and two-leaf hybrid model. ENF = evergreen needleleaf forest, EBF = evergreen broadleaf forest, DBF = deciduous broadleaf forest, SAV = savanna, GRA = grassland, CRO = cropland, SHR = shrubland, and WET = wetland.

distributions of SIF_{sun} and SIF_{shade} were clearly different. High SIF_{sun} was observed in the middle latitude in the Northern Hemisphere, such as the US corn belt and the western Europe (Fig. 3A), while SIF_{shade} was high in the low latitude tropics (Fig. 3B). In addition, these differences can be easily observed from the latitudinal patterns of SIF_{sun} and SIF_{shade} (Fig. 4A). SIF_{shade} was systematically higher than SIF_{sun} in the latitude from -10° to 25°, but lower in other latitudes on average. As a result, EBF (mainly grown in low latitudes) exhibited higher SIF_{shade} than SIF_{sun}, but other vegetation types exhibited higher SIF_{sun} (Fig. 4B).

The spatial differences of SIF_{sun} and SIF_{shade} were mainly related to LAI, the fraction of diffuse radiation, and SZA based on its calculation process (see Section 2.2). We compared the spatial fraction of SIF_{shade}, the fraction of LAI_{shade}, the fraction of $PAR_{diffuse}$, and SZA (Fig. 5). The high fraction of SIF_{shade} (Fig. 5A) in low latitudes were jointly

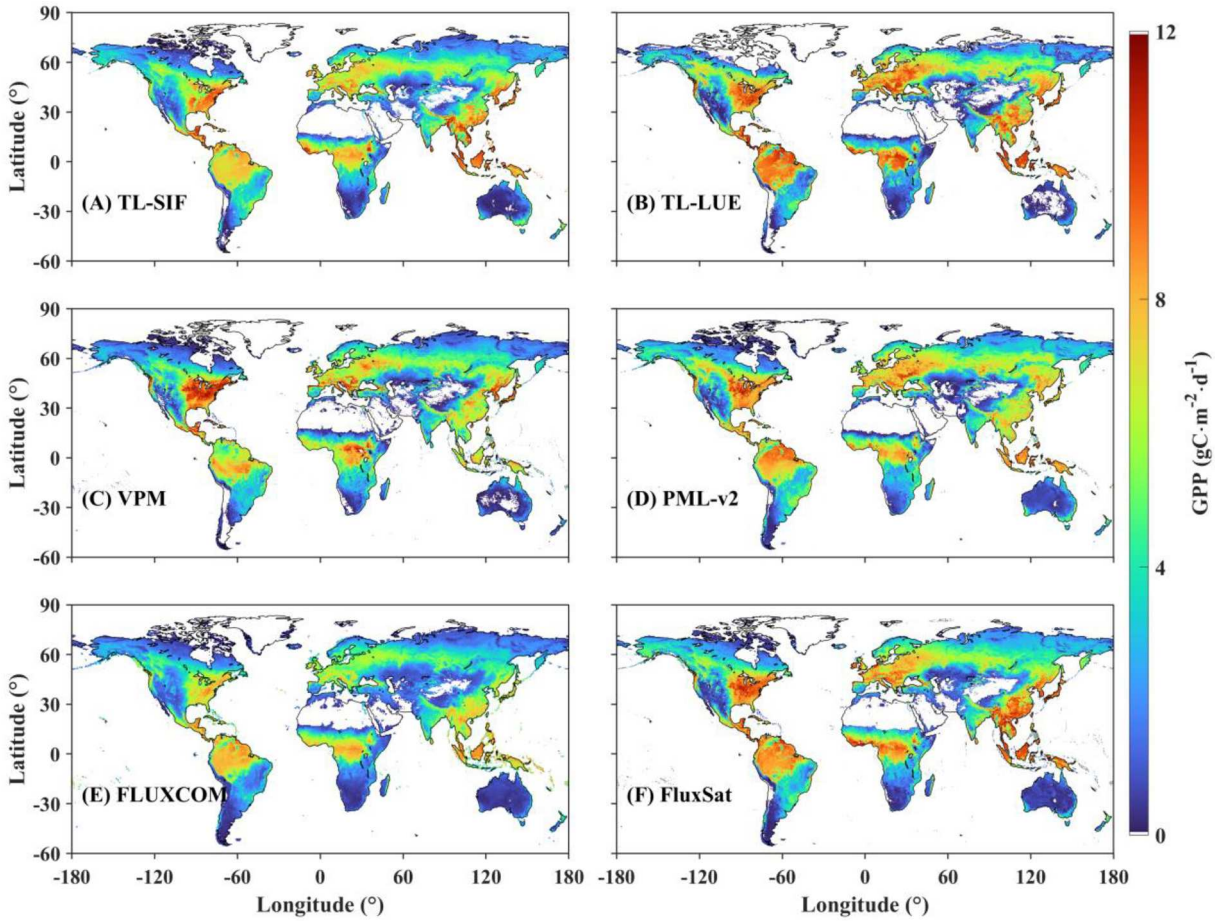

Fig. 9. Global maps of GPP derived from different products: (A) TL-SIF, (B) TL-LUE, (C) VPM, and (D) PML-v2, (E) FLUXCOM, and (F) FluxSat-v2 averaged over May to September in 2018.

determined by the high fraction of LAI_{shade} (Fig. 5B) and $PAR_{diffuse}$ (Fig. 5C). However, we also observed a few high fractions of SIF_{shade} at the northern Russia (Fig. 5A), which would be mainly related to the high fraction of $PAR_{diffuse}$ (Fig. 5C) and SZA (Fig. 5D). These results indicated that the spatial fraction of SIF_{shade} was complex due to the compound effects of multiple factors.

3.2. Relationships between SIF and GPP for sunlit and shaded leaves

Besides the model simulations, TROPOMI SIF and TL-LUE GPP were also used to analyze the SIF-GPP relationships for sunlit and shaded leaves separately (Fig. 6). SIF_{sun} and SIF_{shade} were derived from TROPOMI SIF, and GPP_{sun} and GPP_{shade} were obtained from TL-LUE GPP. We found consistent patterns with the model simulations: nonlinear for sunlit leaves (Fig. 6A) and linear for shaded leaves (Fig. 6B) for all vegetation types. Therefore, it is reasonable to estimate GPP from SIF by considering such model differences between sunlit and shaded leaves. In particular, the nonlinearity of the GPP_{sun} and SIF_{sun} is more clear for forests and other vegetation types than for crops (Fig. A2).

3.3. Accuracy evaluation of GPP estimation models

We compared the performance of three models (a big-leaf-based linear model, a big-leaf-based hyperbolic model, and a two-leaf-based hybrid model) on GPP estimation using the leave-one-site-out crossing validation. If not considering the difference between sunlit and shaded leaves, the big-leaf-based linear model estimated GPP with a R^2 of 0.68 and RMSE of 2.13 $gC{\cdot}m^{-2}{\cdot}d^{-1}$ (Fig. 7A). However, the big-leaf hyperbolic model (Fig. 7B: $R^2 = 0.72$, RMSE = 2.01 $gC{\cdot}m^{-2}{\cdot}d^{-1}$) was slightly better than the linear model, since the linear model ignored the nonlinear relationship between SIF_{sun} and GPP_{sun}. Furthermore, the two-leaf-based hybrid model that considered the difference in sunlit and shaded leaves performed best with a R^2 of 0.77 and RMSE of 1.79 $gC{\cdot}m^{-2}{\cdot}d^{-1}$ (Fig. 7C).

The accuracies of three GPP estimation models for different vegetation types are presented in Fig. 8. In general, the two-leaf-based hybrid model resulted in lower RMSE than the big-leaf-based linear or hyperbolic models. Compared to the big-leaf-based linear model, the RMSE of the two-leaf-based hybrid model reduced by ~0.5 $gC{\cdot}m^{-2}{\cdot}d^{-1}$ for forests (ENF, EBF, and DBF). However, the improvements in RMSE were less than ~0.5 $gC{\cdot}m^{-2}{\cdot}d^{-1}$ for other non-forest vegetation types, and the smallest improvement was obtained for CRO.

3.4. Global estimation of GPP

Furthermore, the two-leaf-based hybrid model was used to estimate the global GPP using SIF_{sun} and SIF_{shade} (denoted as TL-SIF hereafter) due to its best performance. TL-SIF can depict the spatial patterns of vegetation GPP globally, with high values occurring at the low latitude tropics, the US corn belt, the western Europe, and the southeast China (Fig. 9A). We compared the spatial patterns of TL-SIF derived GPP with multiple existing GPP products that were available for the year of 2018 (Fig. 9B-F). In general, TL-SIF GPP exhibited consistent spatial patterns with the current GPP products. The consistency was also demonstrated by high correlations between TL-SIF GPP and other GPP products ($R^2 >$ 0.79, Fig. 10), with the highest correlation TL-SIF GPP and FluxSat GPP ($R^2 = 0.88$, Fig. 10D).

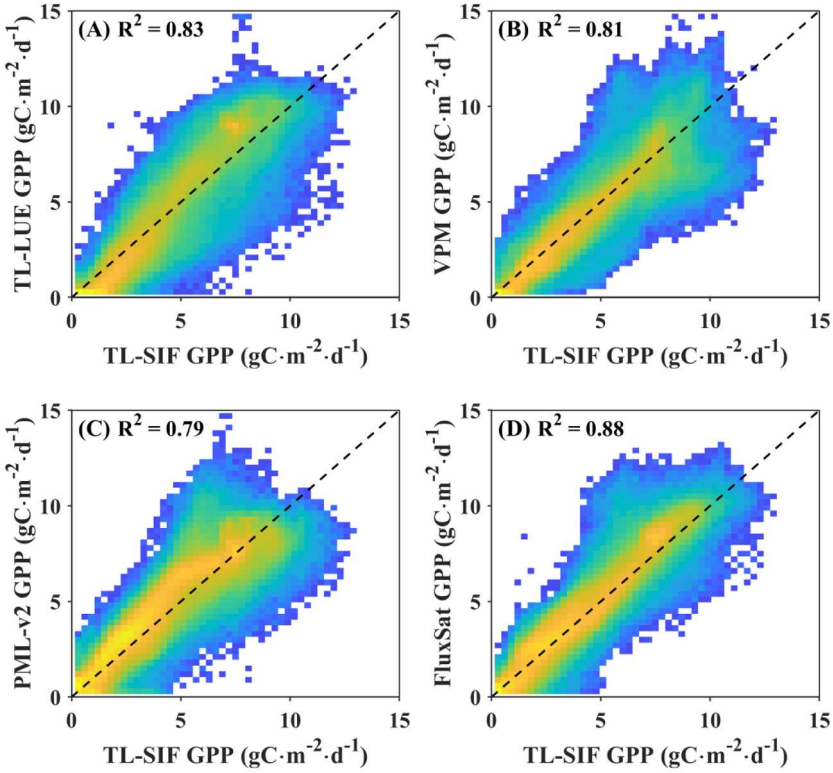

Fig. 10. Comparisons of TL-SIF GPP and GPP estimated from (A) TL-LUE, (B) VPM, (C) PML-v2, and (D) FluxSat-v2. The black dotted lines represent the 1:1 line.

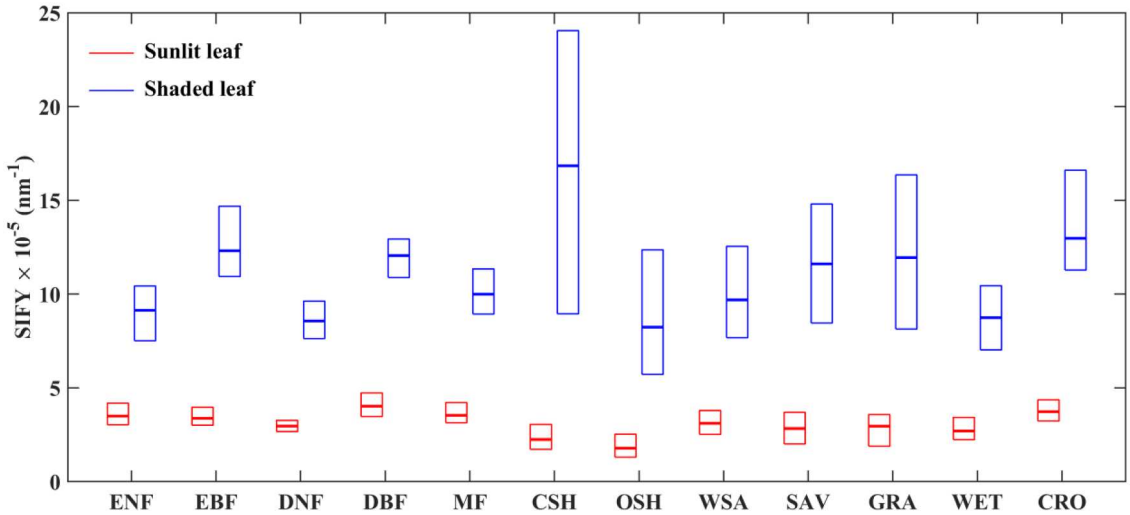

Fig. A1. Box plots of $SIFY_{sun}$ and $SIFY_{shade}$ per vegetation type.

4. Discussion

4.1. Debate on the linear or nonlinear relationships between SIF and GPP

The inherent relationship between SIF and GPP tends to be nonlinear because GPP saturates at high light but SIF does not (Damm et al., 2015; Zhang et al., 2016; Gu et al., 2019; Kim et al., 2021). This nonlinearity between SIF and GPP can be observed from our SCOPE simulations for sunlit leaves with a wide range of illumination (Fig. 2). Although SCOPE is a 1-D model, it is also widely used to characterize the SIF and GPP relationship for forests (Hao et al., 2021). Therefore, it is reliable to conclude that the relationship between SIF and GPP is nonlinear for sunlit leaves (Fig. 2). However, many studies have reported the linear relationships between SIF and GPP over last decades (Frankenberg et al., 2011; Yang et al., 2015; Sun et al., 2017; Miao et al., 2018; Zhang et al., 2020a). Several potential reasons for such a contradictory have been clarified by Magney et al. (2020) who stated that the temporal and spatial aggregations of SIF and GPP strengthen their linearity.

Moreover, the SIF-GPP relationships are also affected by the point when photosynthesis begins to be light-saturated, which mainly depends on photosynthetic pathway (He et al., 2020) and V_{cmax} (Zhang et al., 2016). For example, C_4 plants are less light-saturated compared to C_3 plants (He et al., 2020). In addition, ENF with a low level of V_{cmax} has a small saturation point and hence shows a strong nonlinearity for SIF and GPP (Kim et al., 2021; Liu et al., 2022). On the contrary, linear

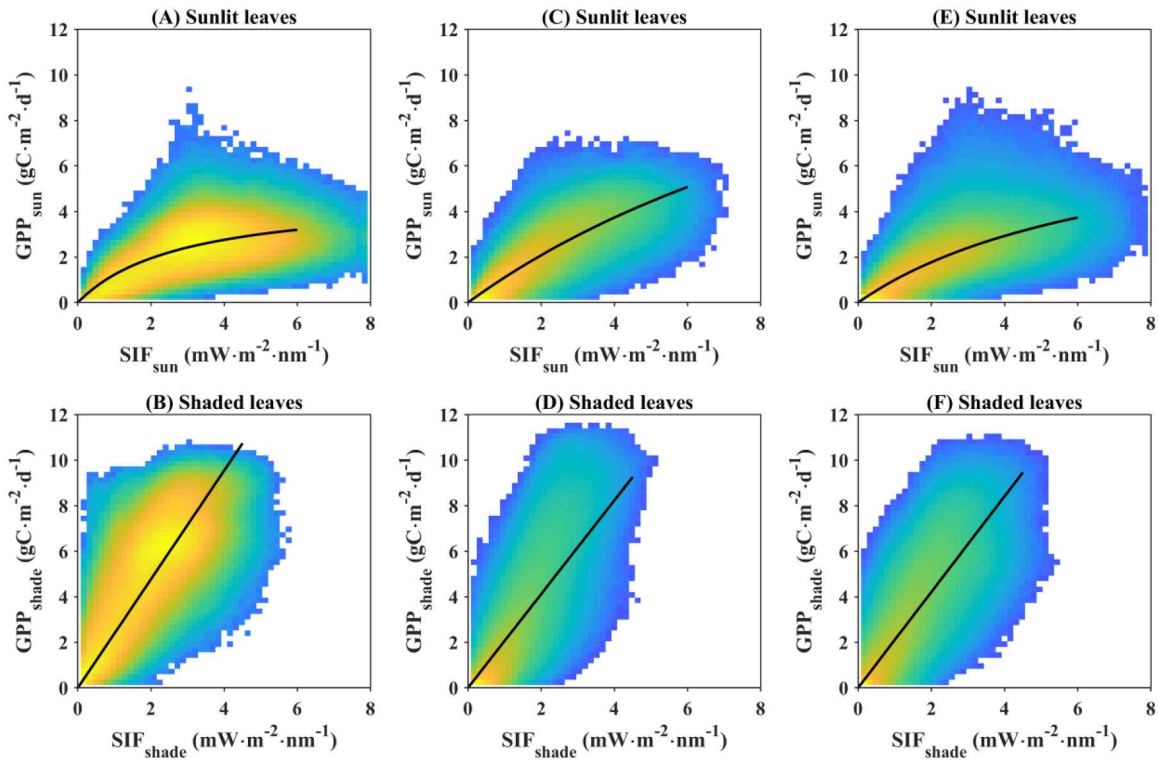

Fig. A2. Similar to Fig. 6 but for (A-B) forests, (C-D) crops, and (E-F) others.

relationships between SIF and GPP are observed for crops with high levels of V_{cmax} (Goulas et al., 2017; Miao et al., 2018; Yang et al., 2018). These results are consistent with the model simulations showing that the degree of nonlinearity and the SIF-GPP model difference between sunlit and shaded leaves are sensitive to the level of V_{cmax} (Fig. 2). Therefore, understanding the spatiotemporal scale and photosynthetic pathway and capacity is crucial for the GPP estimation from SIF using linear or nonlinear relationship.

4.2. The advantage of the two-leaf hybrid model

Regardless of linear or nonlinear models adopted by previous studies, they commonly consider the canopy as a whole (in other words SIF and GPP are the averages of the whole canopy) and ignore the difference in SIF-GPP relationships between sunlit and shaded leaves (as shown by Figs. 2&6). In fact, the canopy can be simply separated into two components: sunlit and shaded leaves (Leuning et al., 1998; Wang and Leuning, 1998). Under clear-sky conditions, sunlit leaves always receive both direct and diffuse radiation and thus are easy to be light saturated (Chen et al., 1999; Bi et al., 2022). However, shaded leaves only received diffuse radiation and transmitted radiation and thus are light-limited (Chen et al., 1999; Bi et al., 2022). Therefore, nonlinear and linear models should be used for sunlit and shaded leaves, respectively, when building the link between SIF and GPP.

In this context, the two-leaf hybrid model is proposed for the first time by taking both sunlit and shaded leaves into consideration (Eq. (13)). On average, the two-leaf hybrid model outperforms traditional big-leaf linear or hyperbolic models (Fig. 7). We also find that the two-leaf hybrid model improves more for forests (Fig. 8). This could be caused by the stronger nonlinearity for forests (Fig. A2A-B) due to the low level of V_{cmax} (40~60 $\mu mol \cdot m^{-2} \cdot s^{-1}$ for ENF and EBF) (He et al., 2019) and also high level of LAI (Liu et al., 2022). Therefore, the separate consideration of sunlit and shaded leaves is necessary. On the contrary, crops have a high level of V_{cmax} (~80 $\mu mol \cdot m^{-2} \cdot s^{-1}$ on average) (He et al., 2019) or (~150 $\mu mol \cdot m^{-2} \cdot s^{-1}$ for soybean) (Zhang et al., 2014), therefore, the nonlinearity of SIF_{sun} and GPP_{sun} is weaker (Fig. A2C-D) and the difference in SIF-GPP relationships is smaller (see the second row in Fig. 2). As a result, a big-leaf linear or hyperbolic model is enough to capture the link between SIF and GPP, leading to the minimal improvement for CRO (Fig. 8).

4.3. Future improvements of GPP based on TL-SIF

The two-leaf hybrid model requires sunlit and shaded SIF as input data, which were derived from TROPOMI SIF in this study. In theory, two observations can be used in Eq. (12) to estimate $SIFY_{sun}$ and $SIFY_{shade}$ and the following SIF_{sun} and SIF_{shade}. The resulting SIF metrics would be affected by the uncertainties in the estimated $APAR_{sun}$ and $APAR_{shade}$ due to the estimation uncertainty from input data (such as LAI and PAR) and several assumptions made for Eqs. (6)–(11). For example, a constant mean leaf-sun angle (60°) was used in this study, although it is a good approximate for the SZA in the range of 20−60° For the other conditions with SZA ⟨ 20° or SZA ⟩ 60°, the suitability of the constant value deserves further study. More accurate estimation of $APAR_{sun}$ and $APAR_{shade}$ would further improve the estimation of SIF_{sun} and SIF_{shade}.

In addition, satellite SIF is retrieved with inherent noises (Köhler et al., 2018a; Sun et al., 2018), which increase the difficulty to derive the accurate estimation of $SIFY_{sun}$ and $SIFY_{shade}$. To mitigate the noise issue, we solved Eq. (12) using the least square method and combined all available observations (after quality control) within a 16-day interval and 1° × 1° moving window. This can effectively reduce the uncertainty in estimating $SIFY_{sun}$ and $SIFY_{shade}$, and the estimates of $SIFY_{sun}$ and $SIFY_{shade}$ can be considered as smoothed values in space and time. The use of a 16-day period partly or completely ignores the variations in $SIFY_{sun}$ and $SIFY_{shade}$ in response to stress. For the sudden drought or flood, the SIF yield varied quickly in response to stress, therefore, this would lead to huge uncertainty of estimated SIF yield and hence SIF. For most regions, the environment at the ecosystem scale (such as 0.2°) varies more slowly compared to a single site where climatic parameters could show high fluctuations. If more accurate SIF retrievals will be

Table A1
Flux sites used in this study. CRO = cropland, DBF = deciduous broadleaf forest, EBF = evergreen broadleaf forest, ENF = evergreen needleleaf forest, GRA = grass, MF = mixed forest, OSH = open shrubland, SAV = savanna, WET = wetland, and WSA = wood savanna.

Site ID	Latitude	Longitude	IGBP	Reference
AR-CCg	−35.9244	−61.1855	GRA	–
CA-LP1	55.1119	−122.8414	ENF	–
CA-SCB	61.3089	−121.2984	WET	–
CA-SMC	63.1534	−123.2522	ENF	–
MX-Aog	26.9968	−108.7892	DBF	–
US-ALQ	46.0308	−89.6067	WET	–
US-BZB	64.6955	−148.3208	WET	–
US-BZF	64.7013	−148.3121	WET	–
US-BZo	64.6936	−148.33	WET	–
US-CdM	37.5241	−109.7471	WSA	–
US-DFC	43.3448	−89.7117	CRO	–
US-EDN	37.6156	−122.114	WET	–
US-EML	63.8784	−149.2536	OSH	(Belshe et al. (2012))
US-HBK	43.9397	−71.7181	DBF	–
US-Ha1	42.5378	−72.1715	DBF	(Urbanski et al. (2007))
US-Ha2	42.5393	−72.1779	ENF	–
US-Hn2	46.6889	−119.4641	GRA	–
US-Hn3	46.6878	−119.4614	OSH	–
US-Ho1	45.2041	−68.7402	ENF	–
US-ICt	68.6063	−149.3041	OSH	–
US-Jo1	32.582	−106.635	OSH	–
US-Jo2	32.5849	−106.6032	OSH	–
US-KFS	39.0561	−95.1907	GRA	–
US-KM4	42.4423	−85.3301	CRO	–
US-KPL	60.5382	−150.5061	WET	–
US-LL1	31.2792	−84.5329	SAV	–
US-Los	46.0827	−89.9792	WET	(Sulman et al. (2009))
US-MMS	39.3232	−86.4131	DBF	(Dragoni et al. (2011))
US-MWF	42.366	−85.3526	MF	–
US-Mo3	39.2311	−92.1497	CRO	–
US-NR1	40.0329	−105.5464	ENF	(Monson et al. (2002))
US-ONA	27.3836	−81.9509	GRA	–
US-Rws	43.1675	−116.7132	OSH	(Flerchinger et al. (2019))
US-Seg	34.3623	−106.7019	GRA	–
US-Ses	34.3349	−106.7442	OSH	–
US-Syv	46.242	−89.3477	MF	(Sulman et al. (2009))
US-Ton	38.4309	−120.966	WSA	(Ma et al. (2007))
US-Vcm	35.8884	−106.5321	ENF	–
US-WCr	45.8059	−90.0799	DBF	(Sulman et al. (2009))
US-Whs	31.7438	−110.0522	OSH	(Scott et al. (2015))
US-Wkg	31.7365	−109.9419	GRA	(Scott et al. (2010))
US-xAE	35.4106	−99.0588	GRA	–
US-xBN	65.154	−147.5026	ENF	–
US-xBR	44.0639	−71.2873	DBF	–
US-xCP	40.8155	−104.7456	GRA	–
US-xDC	47.1617	−99.1066	GRA	–
US-xDJ	63.8811	−145.7514	ENF	–
US-xDL	32.5417	−87.8039	MF	–
US-xHA	42.5369	−72.1727	DBF	–
US-xHE	63.8757	−149.2133	OSH	–
US-xMB	38.2483	−109.3883	OSH	–
US-xNG	46.7697	−100.9154	GRA	–
US-xRM	40.2759	−105.5459	ENF	–
US-xSC	38.8929	−78.1395	DBF	–
US-xSL	40.4619	−103.0293	CRO	–
US-xSR	31.9107	−110.8355	OSH	–
US-xST	45.5089	−89.5864	DBF	–
US-xTA	32.9505	−87.3933	ENF	–
US-xTE	37.0058	−119.006	ENF	–
US-xTR	45.4937	−89.5857	DBF	–
US-xUN	46.2339	−89.5373	MF	–
US-xWD	47.1282	−99.2414	GRA	–
US-xYE	44.9535	−110.5391	ENF	–
AU-Cum	−33.6152	150.7236	EBF	(Beringer et al. (2016))
AU-Lit	−13.179	130.7945	SAV	(Beringer et al. (2016))
AU-Stp	−17.1507	133.3502	GRA	–
AU-Whr	−36.6732	145.0294	EBF	–
AU-Wom	−37.4222	144.0944	EBF	(Hinko-Najera et al. (2017))
AU-Wrr	−43.09501667	146.6545167	EBF	–
AU-Ync	−34.9893	146.2907	GRA	(Yee et al. (2015))
BE-Bra	51.30761	4.51984	MF	(Janssens et al. (2001))
BE-Vie	50.30496	5.99808	MF	(Aubinet et al. (2001))
CH-Lae	47.47808333	8.365	MF	(Etzold et al. (2011))
ES-Abr	38.701839	−6.785881	SAV	(Luo et al. (2018))
ES-LM1	39.94269	−5.778683	SAV	(El-Madany et al. (2018))
ES-LM2	39.934592	−5.775881	SAV	(El-Madany et al. (2018))
FI-Var	67.7549	29.61	ENF	–
FR-Pue	43.7413	3.5957	EBF	(Rambal et al. (2004))
IL-Yat	31.34504459	35.05198851	ENF	–
IT-Tor	45.84444	7.578055	GRA	(Galvagno et al. (2013))

available, a smaller fitting window with a narrower temporal period can be used to reduce the effects of spatial heterogeneity and day-to-day variation.

5. Conclusions

This study proposed an approach to separate the total canopy SIF emission (SIF_{total}) from TROPOMI into their sunlit and shaded components (SIF_{sun} and SIF_{shade}). By comparing SIF and GPP between sunlit and shaded leaves, we found clearly different SIF-GPP relationships between sunlit (nonlinear) and shaded (linear) leaves, which were consistent with the SCOPE model simulations and the theoretical analysis. Therefore, this study proposed a two-leaf hybrid model to consider both linearity and nonlinearity. The two-leaf hybrid model ($R^2 = 0.77$) showed better performances on GPP estimation compared to the big-leaf linear ($R^2 = 0.68$) or hyperbolic ($R^2 = 0.72$) models. We also used this two-leaf hybrid model to estimate the global GPP during the main growing season in Northern Hemisphere and the estimates were highly correlated with several existing GPP products, with R^2 ranging from 0.79 to 0.88. These findings will improve our understanding of the relationship between SIF and GPP and advance application of satellite SIF data to GPP estimation.

Data availability

AmeriFlux data was downloaded from http://ameriflux.ornl.gov/

European Flux was downloaded from http://www.europe-fluxdata.eu/

FLUXCOM GPP was downloaded from http://www.fluxcom.org/

FluxSat v2 GPP was downloaded from https://avdc.gsfc.nasa.gov/pub/tmp/FluxSat_GPP/

MERRA-2 data was downloaded from https://disk.gsfc.nasa.gov/

MODIS-related products were downloaded from https://search.earthdata.nasa.gov/search

OzFlux was downloaded from http://www.ozflux.org.au/

PML v2 GPP was downloaded from http://data.tpdc.ac.cn

TL-LUE v2 GPP was downloaded from https://doi.org/10.5061/dryad.dfn2z352k

TROPOMI SIF was downloaded from https://s5p-troposif.noveltis.fr/

VPM v2 GPP was downloaded from https://doi.org/10.1594/PANGAEA.928381

Declaration of Competing Interest

The authors declare that they have no known competing financial interests or personal relationships that could have appeared to influence the work reported in this paper.

Acknowledgment

This research was supported by the National Natural Science

Foundation of China (42101320, 42125105, 42071388), the National Key Research and Development Program of China (2022YFF1301900), and the Fundamental Research Funds for the Central Universities (0209–14380115). The authors are thankful to the science team members who produced and managed the flux data (AmeriFlux, OzFlux, European Flux) and remote sensing products used in this study. Funding for AmeriFlux data resources was provided by the U.S. Department of Energy's Office of Science. The PML v2 data set is provided by National Tibetan Plateau Data Center (http://data.tpdc.ac.cn).

Appendix

Text A1 the least square method

Eq. (12) can be formulated as Eq. (A1) in the format of matrix, where all parameters have been defined in the context related to Eq. (12). Therefore, the solution ($\hat{x}$) for the unknown parameter X can be calculated using Eq. (A2) for each moving window. Once the process was repeated for all moving windows, the global $SIFY_{sun}$ and $SIFY_{shade}$ was obtained. Fig. A1 shows the boxplots of $SIFY_{sun}$ and $SIFY_{shade}$ for each vegetation type. $SIFY_{sun}$ ranged from 10^{-5} to 5×10^{-5} and $SIFY_{shade}$ showed higher values ($> 0.5 \times 10^{-4}$). This is expected that $SIFY_{sun}$ at the high illumination is lower than $SIFY_{shade}$ at the low illumination.

$$Y = \mathrm{AXE}$$

$$Y = \begin{bmatrix} SIF^1_{total} \\ \vdots \\ SIF^N_{total} \end{bmatrix}$$

$$A = \begin{bmatrix} APAR^1_{sun} & APAR^1_{shade} \\ & \vdots \\ APAR^N_{sun} & APAR^N_{shade} \end{bmatrix} \tag{A1}$$

$$X = [\, SIFY_{sun} \quad SIFY_{shade} \,]$$

$$\hat{x} = \left(A^T A\right)^{-1} A^T Y \tag{A2}$$

References

Aubinet, M., Chermanne, B., Vandenhaute, M., Longdoz, B., Yernaux, M., Laitat, E., 2001. Long term carbon dioxide exchange above a mixed forest in the Belgian Ardennes. Agric. For. Meteorol. 108, 293–315.

Badgley, G., Anderegg, L.D.L., Berry, J.A., Field, C.B., 2019. Terrestrial gross primary production: using NIR_V to scale from site to globe. Glob Chang. Biol. 25, 3731–3740.

Badgley, G., Field, C.B., Berry, J.A., 2017. Canopy near-infrared reflectance and terrestrial photosynthesis. Sci. Adv. 3, e1602244.

Belshe, E., Schuur, E., Bolker, B., Bracho, R., 2012. Incorporating spatial heterogeneity created by permafrost thaw into a landscape carbon estimate. J. Geophys. Res. Biogeosci. 117.

Beringer, J., Hutley, L.B., McHugh, I., Arndt, S.K., Campbell, D., Cleugh, H.A., et al., 2016. An introduction to the Australian and New Zealand flux tower network – OzFlux. Biogeosciences 13, 5895–5916.

Bi, W., He, W., Zhou, Y., Ju, W., Liu, Y., Liu, Y., et al., 2022. A global 0.05° dataset for gross primary production of sunlit and shaded vegetation canopies from 1992 to 2020. Sci. Data 9, 213.

Bodesheim, P., Jung, M., Gans, F., Mahecha, M.D., Reichstein, M., 2018. Upscaled diurnal cycles of land–atmosphere fluxes: a new global half-hourly data product. Earth Syst. Sci. Data 10, 1327–1365.

Chen, J.M., Liu, J., Cihlar, J., Goulden, M., 1999. Daily canopy photosynthesis model through temporal and spatial scaling for remote sensing applications. Ecol. Modell. 124, 99–119.

Damm, A., Guanter, L., Paul-Limoges, E., van der Tol, C., Hueni, A., Buchmann, N., et al., 2015. Far-red sun-induced chlorophyll fluorescence shows ecosystem-specific relationships to gross primary production: an assessment based on observational and modeling approaches. Remote Sens. Environ. 166, 91–105.

Dragoni, D., Schmid, H.P., Wayson, C.A., Potter, H., Grimmond, C.S.B., Randolph, J.C., 2011. Evidence of increased net ecosystem productivity associated with a longer vegetated season in a deciduous forest in south-central Indiana, USA. Glob Chang. Biol. 17, 886–897.

El-Madany, T.S., Reichstein, M., Perez-Priego, O., Carrara, A., Moreno, G., Pilar Martín, M., et al., 2018. Drivers of spatio-temporal variability of carbon dioxide and energy fluxes in a Mediterranean savanna ecosystem. Agric. For. Meteorol. 262, 258–278.

Etzold, S., Ruehr, N.K., Zweifel, R., Dobbertin, M., Zingg, A., Pluess, P., et al., 2011. The carbon balance of two contrasting mountain forest ecosystems in Switzerland: similar annual trends, but seasonal differences. Ecosystems 14, 1289–1309.

Flerchinger, G.N., Fellows, A.W., Seyfried, M.S., Clark, P.E., Lohse, K.A., 2019. Water and carbon fluxes along an elevational gradient in a sagebrush ecosystem. Ecosystems 23, 246–263.

Frankenberg, C., Fisher, J.B., Worden, J., Badgley, G., Saatchi, S.S., Lee, J.E., et al., 2011. New global observations of the terrestrial carbon cycle from GOSAT: patterns of plant fluorescence with gross primary productivity. Geophys. Res. Lett. 38, 351–365.

Frankenberg, C., O'Dell, C., Berry, J., Guanter, L., Joiner, J., Koehler, P., et al., 2014. Prospects for chlorophyll fluorescence remote sensing from the Orbiting Carbon Observatory-2. Remote Sens. Environ. 147, 1–12.

Galvagno, M., Wohlfahrt, G., Cremonese, E., Rossini, M., Colombo, R., Filippa, G., et al., 2013. Phenology and carbon dioxide source/sink strength of a subalpine grassland in response to an exceptionally short snow season. Environ. Res. Lett. 8, 025008.

Gelaro, R., McCarty, W., Suárez, M.J., Todling, R., Molod, A., Takacs, L., et al., 2017. The Modern-Era Retrospective Analysis for Research and Applications, Version 2 (MERRA-2). J. Clim. 30, 5419–5454.

Genty, B., Briantais, J.M., Baker, N.R., 1989. The relationship between the quantum yield of photosynthetic electron transport and quenching of chlorophyll fluorescence. Biochim. Biophys. Gen. Sub. 990, 87–92.

Goulas, Y., Fournier, A., Daumard, F., Champagne, S., Ounis, A., Marloie, O., Moya, I., 2017. Gross primary production of a wheat canopy relates stronger to far red than to red solar-induced chlorophyll fluorescence. Remote Sens (Basel) 9, 97.

Gu, L., Han, J., Wood, J.D., Chang, C.Y.Y., Sun, Y., 2019. Sun-induced Chl fluorescence and its importance for biophysical modeling of photosynthesis based on light reactions. New Phytol. 223, 1179–1191.

Guan, X., Chen, J.M., Shen, H., Xie, X., 2021. A modified two-leaf light use efficiency model for improving the simulation of GPP using a radiation scalar. Agric. For. Meteorol. 307, 108546.

Guanter, L., Bacour, C., Schneider, A., Aben, I., van Kempen, T.A., Maignan, F., et al., 2021. The TROPOSIF global sun-induced fluorescence dataset from the Sentinel-5P TROPOMI mission. Earth System Science Data 13, 5423–5440.

Guanter, L., Zhang, Y., Jung, M., Joiner, J., Voigt, M., Berry, J.A., et al., 2014. Global and Time-Resolved Monitoring of Crop Photosynthesis With Chlorophyll Fluorescence, 111. Proceedings of the National Academy of Sciences of the United States of America, pp. E1327–E1333.

Hao, D., Asrar, G.R., Zeng, Y., Yang, X., Li, X., Xiao, J., et al., 2021. Potential of hotspot solar-induced chlorophyll fluorescence for better tracking terrestrial photosynthesis. Global Change Biology.

He, L., Chen, J.M., Liu, J., Mo, G., Joiner, J., 2017. Angular normalization of GOME-2 Sun-induced chlorophyll fluorescence observation as a better proxy of vegetation productivity. Geophys. Res. Lett. 44, 5691–5699.

He, L., Chen, J.M., Liu, J., Zheng, T., Wang, R., Joiner, J., et al., 2019. Diverse photosynthetic capacity of global ecosystems mapped by satellite chlorophyll fluorescence measurements. Remote Sens. Environ. 232, 111344.
He, L., Chen, J.M., Pisek, J., Schaaf, C.B., Strahler, A.H., 2012. Global clumping index map derived from the MODIS BRDF product. Remote Sens. Environ. 119, 118–130.
He, L., Magney, T., Dutta, D., Yin, Y., Köhler, P., Grossmann, K., et al., 2020. From the ground to space: using solar-induced chlorophyll fluorescence to estimate crop productivity. Geophys. Res. Lett. 47, e2020GL087474.
Hinko-Najera, N., Isaac, P., Beringer, J., van Gorsel, E., Ewenz, C., McHugh, I., et al., 2017. Net ecosystem carbon exchange of a dry temperate eucalypt forest. Biogeosciences 14, 3781–3800.
Janssens, I.A., Kowalski, A.S., Ceulemans, R., 2001. Forest floor CO_2 fluxes estimated by eddy covariance and chamber-based model. Agric. For. Meteorol. 106, 61–69.
Joiner, J., Yoshida, Y., 2020. Satellite-based reflectances capture large fraction of variability in global gross primary production (GPP) at weekly time scales. Agric. For. Meteorol. 291, 108092.
Joiner, J., Yoshida, Y., Zhang, Y., Duveiller, G., Jung, M., Lyapustin, A., et al., 2018. Estimation of terrestrial global gross primary production (GPP) with satellite data-driven models and eddy covariance flux data. Remote Sens (Basel) 10, 1346.
Kim, J., Ryu, Y., Dechant, B., Lee, H., Kim, H.S., Kornfeld, A., Berry, J.A., 2021. Solar-induced chlorophyll fluorescence is non-linearly related to canopy photosynthesis in a temperate evergreen needleleaf forest during the fall transition. Remote Sens. Environ. 258, 112362.
Köhler, P., Frankenberg, C., Magney, T.S., Guanter, L., Joiner, J., Landgraf, J., 2018a. Global retrievals of Solar-Induced Chlorophyll Fluorescence with TROPOMI: first results and intersensor comparison to OCO-2. Geophys. Res. Lett. 45, 10456–10463.
Köhler, P., Guanter, L., Kobayashi, H., Walther, S., Yang, W., 2018b. Assessing the potential of sun-induced fluorescence and the canopy scattering coefficient to track large-scale vegetation dynamics in Amazon forests. Remote Sens. Environ. 204, 769–785.
Krause, G., Weis, E., 1991. Chlorophyll fluorescence and photosynthesis: the basics. Annu. Rev. Plant Biol. 42, 313–349.
Lee, J.E., Berry, J.A., van der Tol, C., Yang, X., Guanter, L., Damm, A., et al., 2015. Simulations of chlorophyll fluorescence incorporated into the Community Land Model version 4. Glob Chang Biol 21, 3469–3477.
Leuning, R., Dunin, F.X., Wang, Y.P., 1998. A two-leaf model for canopy conductance, photosynthesis and partitioning of available energy. II. Comparison with measurements. Agric. For. Meteorol. 91, 113–125.
Li, R., Lombardozzi, D., Shi, M., Frankenberg, C., Parazoo, N.C., Köhler, P., et al., 2022. Representation of leaf-to-canopy radiative transfer processes improves simulation of far-red solar-induced chlorophyll fluorescence in the community land model version 5. J. Adv. Model. Earth Syst. 14, e2021MS002747.
Li, X., Xiao, J., He, B., Arain, M.A., Beringer, J., Desai, A.R., et al., 2018. Solar-induced chlorophyll fluorescence is strongly correlated with terrestrial photosynthesis for a wide variety of biomes: first global analysis based on OCO-2 and flux tower observations. Glob Chang Biol 24, 3990–4008.
Li, X., Xiao, J.F., 2019. Mapping photosynthesis solely from solar-induced chlorophyll fluorescence: a global, fine-resolution dataset of gross primary production derived from OCO-2. Remote Sens (Basel) 11, 2563.
Liu, X., Liu, L., Hu, J., Guo, J., Du, S., 2020. Improving the potential of red SIF for estimating GPP by downscaling from the canopy level to the photosystem level. Agric. For. Meteorol. 281, 107846.
Liu, Y., Chen, J.M., He, L., Zhang, Z., Wang, R., Rogers, C., et al., 2022. Non-linearity between gross primary productivity and far-red solar-induced chlorophyll fluorescence emitted from canopies of major biomes. Remote Sens. Environ. 271, 112896.
Luo, Y., El-Madany, T.S., Filippa, G., Ma, X., Ahrens, B., Carrara, A., et al., 2018. Using near-infrared-enabled digital repeat photography to track structural and physiological phenology in Mediterranean tree–grass ecosystems. Remote Sens. 10, 1293 (Basel).
Lyapustin, A., Martonchik, J., Wang, Y., Laszlo, I., Korkin, S., 2011. Multiangle implementation of atmospheric correction (MAIAC): 1. Radiative transfer basis and look-up tables. J. Geophys. Res. Atmos. 116, D03210.
Lyapustin, A., Wang, Y., Korkin, S., Huang, D., 2018. MODIS Collection 6 MAIAC algorithm. Atmos. Meas. Tech. 11, 5741–5765.
Ma, S.Y., Baldocchi, D.D., Xu, L.K., Hehn, T., 2007. Inter-annual variability in carbon dioxide exchange of an oak/grass savanna and open grassland in California. Agric. For. Meteorol. 147, 157–171.
MacBean, N., Maignan, F., Bacour, C., Lewis, P., Peylin, P., Guanter, L., et al., 2018. Strong constraint on modelled global carbon uptake using solar-induced chlorophyll fluorescence data. Sci. Rep. 8, 1973.
Magney, T.S., Barnes, M.L., Yang, X., 2020. On the covariation of chlorophyll fluorescence and photosynthesis across scales. Geophys. Res. Lett. 47, e2020GL091098.
Maguire, A.J., Eitel, J.U.H., Griffin, K.L., Magney, T.S., Long, R.A., Vierling, L.A., et al., 2020. On the functional relationship between fluorescence and photochemical yields in complex evergreen needleleaf canopies. Geophys. Res. Lett. 47, e2020GL087858.
Meroni, M., Rossini, M., Guanter, L., Alonso, L., Rascher, U., Colombo, R., Moreno, J., 2009. Remote sensing of solar-induced chlorophyll fluorescence: review of methods and applications. Remote Sens. Environ. 113, 2037–2051.
Miao, G., Guan, K., Yang, X., Bernacchi, C.J., Berry, J.A., DeLucia, E.H., et al., 2018. Sun-induced chlorophyll fluorescence, photosynthesis, and light use efficiency of a soybean field from seasonally continuous measurements. J. Geophys. Res. Biogeosci. 123, 610–623.
Monson, R., Turnipseed, A., Sparks, J., Harley, P., Scott-Denton, L., Sparks, K., Huxman, T., 2002. Carbon sequestration in a high-elevation, subalpine forest. Glob Chang. Biol. 8, 459–478.
Myneni, R.B., Hoffman, S., Knyazikhin, Y., Privette, J.L., Glassy, J., Tian, Y., et al., 2002. Global Products of Vegetation Leaf Area and Fraction Absorbed PAR from Year One of MODIS Data, 83. Remote Sensing of Environment, pp. 214–231.
Norton, A.J., Rayner, P.J., Koffi, E.N., Scholze, M., 2018. Assimilating solar-induced chlorophyll fluorescence into the terrestrial biosphere model BETHY-SCOPE v1. 0: model description and information content. Geosci. Model. Dev. 11, 1517–1536.
Pierrat, Z., Magney, T., Parazoo, N.C., Grossmann, K., Bowling, D.R., Seibt, U., et al., 2022. Diurnal and seasonal dynamics of solar-induced chlorophyll fluorescence, vegetation indices, and gross primary productivity in the boreal forest. J. Geophys. Res. Biogeosci. 127, e2021JG006588.
Porcar-Castell, A., Malenovský, Z., Magney, T., Van Wittenberghe, S., Fernández-Marín, B., Maignan, F., et al., 2021. Chlorophyll a fluorescence illuminates a path connecting plant molecular biology to Earth-system science. Nat. Plants 7, 998–1009.
Porcar-Castell, A., Tyystjarvi, E., Atherton, J., van der Tol, C., Flexas, J., Pfundel, E.E., et al., 2014. Linking chlorophyll a fluorescence to photosynthesis for remote sensing applications: mechanisms and challenges. J. Exp. Bot. 65, 4065–4095.
Pury, D., Farquhar, G.D., 1997. Simple scaling of photosynthesis from leaves to canopies without the errors of big-leaf models. Plant Cell Environ. 20, 537–557.
Rambal, S., Joffre, R., Ourcival, J., Cavender-Bares, J., Rocheteau, A., 2004. The growth respiration component in eddy CO_2 flux from a Quercus ilex mediterranean forest. Glob Chang. Biol. 10, 1460–1469.
Reichstein, M., Falge, E., Baldocchi, D., Papale, D., Aubinet, M., Berbigier, P., et al., 2005. On the separation of net ecosystem exchange into assimilation and ecosystem respiration: review and improved algorithm. Glob Chang. Biol. 11, 1424–1439.
Scott, R.L., Biederman, J.A., Hamerlynck, E.P., Barron-Gafford, G.A., 2015. The carbon balance pivot point of southwestern U.S. semiarid ecosystems: insights from the 21st century drought. J. Geophys. Res. Biogeosci. 120, 2612–2624.
Scott, R.L., Hamerlynck, E.P., Jenerette, G.D., Moran, M.S., Barron-Gafford, G.A., 2010. Carbon dioxide exchange in a semidesert grassland through drought-induced vegetation change. J. Geophys. Res. Biogeosci. 115, G03026.
Sulman, B., Desai, A., Cook, B., Saliendra, N., Mackay, D., 2009. Contrasting carbon dioxide fluxes between a drying shrub wetland in Northern Wisconsin, USA, and nearby forests. Biogeosciences 6, 1115–1126.
Sun, Y., Frankenberg, C., Jung, M., Joiner, J., Guanter, L., Köhler, P., Magney, T., 2018. Overview of Solar-Induced chlorophyll Fluorescence (SIF) from the Orbiting Carbon Observatory-2: retrieval, cross-mission comparison, and global monitoring for GPP. Remote Sens. Environ. 209, 808–823.
Sun, Y., Frankenberg, C., Wood, J.D., Schimel, D.S., Jung, M., Guanter, L., et al., 2017. OCO-2 advances photosynthesis observation from space via solar-induced chlorophyll fluorescence. Science 358, eaam5747.
Sun, Y., Gu, L., Wen, J., van der Tol, C., Porcar-Castell, A., Joiner, J., et al., 2023. From remotely sensed solar-induced chlorophyll fluorescence to ecosystem structure, function, and service: part I—Harnessing theory. Glob Chang. Biol. 29, 2926–2952.
Tramontana, G., Jung, M., Schwalm, C.R., Ichii, K., Camps-Valls, G., Raduly, B., et al., 2016. Predicting carbon dioxide and energy fluxes across global FLUXNET sites with regression algorithms. Biogeosciences 13, 4291–4313.
Urbanski, S., Barford, C., Wofsy, S., Kucharik, C., Pyle, E., Budney, J., et al., 2007. Factors controlling CO_2 exchange on timescales from hourly to decadal at Harvard Forest. J. Geophys. Res. Biogeosci. 112, G02020.
van der Tol, C., Berry, J.A., Campbell, P.K.E., Rascher, U., 2014. Models of fluorescence and photosynthesis for interpreting measurements of solar-induced chlorophyll fluorescence. J. Geophys. Res. Biogeosci. 119, 2312–2327.
van der Tol, C., Verhoef, W., Rosema, A., 2009a. A model for chlorophyll fluorescence and photosynthesis at leaf scale. Agric. For. Meteorol. 149, 96–105.
van der Tol, C., Verhoef, W., Timmermans, J., Verhoef, A., Su, Z., 2009b. An integrated model of soil-canopy spectral radiances, photosynthesis, fluorescence, temperature and energy balance. Biogeosciences 6, 3109–3129.
Wang, Y.P., Leuning, R., 1998. A two-leaf model for canopy conductance, photosynthesis and partitioning of available energy I Model description and comparison with a multi-layered model. Agric. For. Meteorol. 91, 89–111.
Xie, X., Li, A., 2020. An adjusted two-leaf light use efficiency model for improving GPP simulations over mountainous areas. J. Geophys. Res. Atmos. 125, e2019JD031702.
Yang, K., Ryu, Y., Dechant, B., Berry, J.A., Hwang, Y., Jiang, C., et al., 2018. Sun-induced chlorophyll fluorescence is more strongly related to absorbed light than to photosynthesis at half-hourly resolution in a rice paddy. Remote Sens. Environ. 216, 658–673.
Yang, P., Prikaziuk, E., Verhoef, W., van der Tol, C., 2021. SCOPE 2.0: a model to simulate vegetated land surface fluxes and satellite signals. Geosci. Model. Dev. 14, 4697–4712.
Yang, P., van der Tol, C., 2018. Linking canopy scattering of far-red sun-induced chlorophyll fluorescence with reflectance. Remote Sens. Environ. 209, 456–467.
Yang, X., Tang, J., Mustard, J.F., Lee, J.E., Rossini, M., Joiner, J., et al., 2015. Solar-induced chlorophyll fluorescence that correlates with canopy photosynthesis on diurnal and seasonal scales in a temperate deciduous forest. Geophys. Res. Lett. 42, 2977–2987.
Yee, M.S., Pauwels, V.R., Daly, E., Beringer, J., Rüdiger, C., McCabe, M.F., Walker, J.P., 2015. A comparison of optical and microwave scintillometers with eddy covariance derived surface heat fluxes. Agric. For. Meteorol. 213, 226–239.
Yu, L., Wen, J., Chang, C.Y., Frankenberg, C., Sun, Y., 2019. High-resolution global contiguous SIF of OCO-2. Geophys. Res. Lett. 46, 1449–1458.

Zeng, Y., Badgley, G., Dechant, B., Ryu, Y., Chen, M., Berry, J., 2019. A practical approach for estimating the escape ratio of near-infrared solar-induced chlorophyll fluorescence. Remote Sens. Environ. 232, 211209.

Zhang, Y., Kong, D., Gan, R., Chiew, F.H.S., McVicar, T.R., Zhang, Q., Yang, Y., 2019. Coupled estimation of 500 m and 8-day resolution global evapotranspiration and gross primary production in 2002–2017. Remote Sens. Environ. 222, 165–182.

Zhang, Y., Xiao, X., Wu, X., Zhou, S., Zhang, G., Qin, Y., Dong, J., 2017. A global moderate resolution dataset of gross primary production of vegetation for 2000-2016. Sci. Data 4, 170165.

Zhang, Y.G., Guanter, L., Berry, J.A., Joiner, J., van der Tol, C., Huete, A., et al., 2014. Estimation of vegetation photosynthetic capacity from space-based measurements of chlorophyll fluorescence for terrestrial biosphere models. Glob Chang. Biol. 20, 3727–3742.

Zhang, Y.G., Guanter, L., Berry, J.A., van der Tol, C., Yang, X., Tang, J., Zhang, F., 2016. Model-based analysis of the relationship between sun-induced chlorophyll fluorescence and gross primary production for remote sensing applications. Remote Sens. Environ. 187, 145–155.

Zhang, Z.Y., Zhang, Y., Chen, J.M., Ju, W., Migliavacca, M., El-Madany, T.S., 2021. Sensitivity of estimated total canopy SIF emission to remotely sensed LAI and BRDF products. J. Remote Sens. 2021, 9795837.

Zhang, Z.Y., Zhang, Y.G., Porcar-Castell, A., Joiner, J., Guanter, L., Yang, X., et al., 2020a. Reduction of structural impacts and distinction of photosynthetic pathways in a global estimation of GPP from space-borne solar-induced chlorophyll fluorescence. Remote Sens. Environ. 240, 111722.

Zhang, Z.Y., Zhang, Y.G., Zhang, Y., Chen, J.M., 2020b. Correcting clear-sky bias in gross primary production modeling from satellite solar-induced chlorophyll fluorescence data. J. Geophys. Res. Biogeosci. 125, e2020JG005822.

Zhou, Y., Wu, X., Ju, W., Chen, J.M., Wang, S., Wang, H., et al., 2016. Global parameterization and validation of a two-leaf light use efficiency model for predicting gross primary production across FLUXNET sites. J. Geophys. Res. Biogeosci. 121, 1045–1072.